

Electromagnetic Property Analysis of a Bearingless Induction Motor Using Amorphous Alloy Material

Ting Xu¹, Zebin Yang^{1, *}, Xiaodong Sun², and Jingjing Jia¹

Abstract—A bearingless induction motor (BL-IM) is a new type of motor integrating suspension and rotation functions. Higher requirements are put forward for its suspension performance. Due to the material advantages of a new type of amorphous alloy with high magnetic conductivity, low loss, and low coercivity, it is considered to be used in the BL-IM rotor to reduce iron loss and improve the electromagnetic performance of the BL-IM. Finite element analysis software is used to analyze the performance of two different kinds of motors with the rotors made of conventional silicon steel and amorphous alloy, respectively. The magnetic field density distribution, torque, speed, and radial force are compared between the two motors. The results show that the speed of amorphous alloy motor increases faster, and the rotor has better suspension characteristics. Moreover, the amorphous alloy material has a smaller density; the material properties can effectively reduce the weight of the motor; it is beneficial to the operation of the BL-IM in special environments.

1. INTRODUCTION

A bearingless motor is a new type of motor, which offers frictionless wear, corrosion resistance, no lubrication, and high-speed and ultra-high-speed operation [1–5]. Compared with other motors, bearingless induction motors (BL-IMs) possess the advantages of simple structure, solid and reliable structure, uniform air gap, low cost, low teeth groove pulsation torque, etc. A new electrical transmission scheme is provided for the development of special transmission equipment towards high, precise, and sharp direction, such as automation of production equipment, high-speed centrifugal pump, and flywheel energy storage [6–10].

Stator and rotor core of a traditional motor is mostly made of silicon steel material, but its inherent characteristics can bring big loss, heat, and other problems. As a new type of soft magnetic material, amorphous alloy material [11–17] has excellent electromagnetic properties, like high permeability, low coercivity, and low loss [30, 31]. Applying amorphous alloy material to the motor core instead of the conventional silicon steel sheet material can significantly reduce the iron consumption of the motor, improve the efficiency of the motor, and achieve remarkable energy saving effect. Especially for high frequency motor applications where iron consumption is the main part, such as high speed spindle motor and fan, the energy saving effect is better, and it has a broad application prospect. At the same time, its density is lower than that of silicon steel material, and its weight is less. As a new type of motor integrating suspension and rotation functions, higher requirements are put forward in BL-IM for its suspension performance. Therefore, the application of amorphous alloy material in the BL-IM rotor can reduce the vibration amplitude of the motor rotor and obtain better rotor suspension performance. Moreover, it can better meet the requirements of the BL-IM high-speed and ultra-high-speed operating environment, as well as the operation of special fields such as life science. In [11], the

Received 26 June 2021, Accepted 4 August 2021, Scheduled 13 August 2021

* Corresponding author: Zebin Yang (zbyang@ujs.edu.cn).

¹ School of Electrical Information Engineering, Jiangsu University, Zhenjiang 212013, China. ² Automotive Engineering Research Institute, Jiangsu University, Zhenjiang 212013, China.

radial electromagnetic vibration of amorphous stator core was analyzed and studied in the permanent magnet motor, and the vibration of conventional silicon steel core and amorphous core were compared. The results showed that the vibration of amorphous core was less than that of silicon steel core under the same other conditions, which provides a theoretical basis for the design of high efficiency motor. In [12], a new type of ultra-thick amorphous strip was studied. The annealed amorphous alloy showed excellent soft magnetic properties and good ductility. The newly developed amorphous soft magnetic alloys combined high GFA, excellent ductility, and low core loss, which made them attractive candidates for magnetic applications in high frequency and high-speed electronic devices. As mentioned in [16], due to their superior strength, high elasticity, and excellent corrosion resistance, amorphous alloy has attracted the attention of many researchers. It has become an important material for precision machinery, energy conversion, information processing, and aerospace components. Therefore, further promotion of the amorphous alloy materials application range can provide more diversified choices for the market, further meet the market demand, and thus achieve higher economic benefits.

The performance improvement is studied in the BL-IM rotor with amorphous alloy material. Finite element analysis software is used to calculate and analyze the performance of silicon steel material and amorphous alloy material for the rotor core. The magnetic density distributions, torques, speeds, and radial forces of the two materials are compared under no-load and on-load operating conditions. Combined with the advantages of the amorphous alloy material, the feasibility of the amorphous alloy motor is verified.

2. THE BL-IM SUSPENSION PRINCIPLE

The stator of the BL-IM is simultaneously wound with two sets of windings, torque winding with pole pairs of P_1 and suspension force winding with pole pairs of P_2 . The following three conditions [18, 19] are satisfied by the two sets of windings, and the motor can achieve effective suspension operation.

- 1) $P_1 = P_2 \pm 1$.
- 2) Angular frequency $\omega_1 = \omega_2$.
- 3) The rotation magnetic fields are in the same direction.

The nonuniform distribution of the motor's air-gap magnetic field is controlled through the interaction of currents in the two sets of windings, thus generating controlled radial force acting on the rotor to realize rotation and levitation [20, 21]. The basic parameters of the BL-IM analyzed are shown in Table 1.

The radial suspension force generation principle of the BL-IM is shown in Fig. 1. The four-pole torque winding and two-pole suspension force winding are superposed in the stator slots. Currents

Table 1. The parameters of the BL-IM.

Parameters	Torque winding	Suspension force winding
Rated current (A)	2.86	1.43
Stator resistance (Ω)	2.01	1.03
Rotor resistance (Ω)	11.48	0.075
Constant and rotor mutual Inductance (mH)	158.56	9.32
Stator leakage inductance (mH)	4.45	2.67
Rotor leakage inductance (mH)	9.22	5.42
Rotational inertia ($\text{g}\cdot\text{m}^2$)	7.69	7.69
Rotor weight (kg)	2.85	2.85
Diameter of stator (mm)	98	98
Core length (mm)	105	105
Pole-pairs	2	1

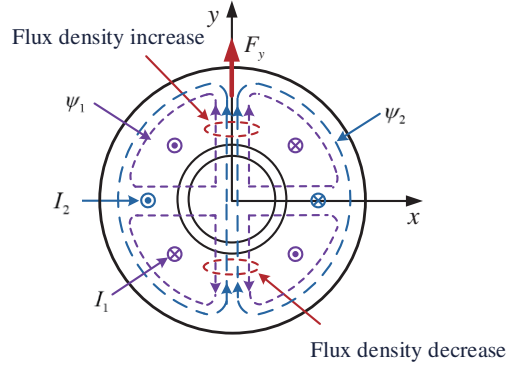


Figure 1. Generation principle of radial suspension force for the BL-IM.

I_1 and I_2 are switched on in two sets of windings under non-load operation, respectively, producing magnetic chain ψ_1 and ψ_2 as shown in Fig. 1. In the upper-side of the air gap, ψ_1 and ψ_2 are in the same direction, so the air gap flux density is increased. In the lower-side of the air gap, ψ_1 and ψ_2 are in the opposite directions, so the air gap flux density is reduced. Thus, the radial suspension force F_y along the positive y -axis is generated. Similarly, if the radial suspension force along the x -axis direction is considered to obtain, the current perpendicular to I_2 can be passed through the suspension force winding. Therefore, the magnitude and direction of the suspension force can be controlled by changing the current in the suspension force winding to achieve stable suspension of the BL-IM rotor.

The radial suspension force is composed of Lorentz force and Maxwell force. In order to generate greater suspension force under the same condition and control the suspension of the rotor more effectively, Lorentz force and Maxwell force are generally required to be in the same direction. In this case, the suspension forces in x and y directions of the motor are

$$\begin{cases} F_x = K (i_{s2\alpha}\psi_{1\alpha} + i_{s2\beta}\psi_{1\beta}) \\ F_y = K (i_{s2\beta}\psi_{1\alpha} - i_{s2\alpha}\psi_{1\beta}) \end{cases} \quad (1)$$

where $K = \pi P_1 P_2 L_{2m} / 18lr\mu_0 W_1 W_2$; F_x and F_y are the radial suspension force components, respectively; $i_{s2\alpha}$ and $i_{s2\beta}$ are the suspension winding stator currents on α - β axis, respectively; $\psi_{1\alpha}$ and $\psi_{1\beta}$ are the suspension winding air gap flux linkages on the α - β axis, respectively; P_1 and P_2 are the pole pairs of torque winding and suspension winding, respectively; L_{2m} is the mutual inductance of suspension winding; l is the effective length of the core; μ_0 is the vacuum magnetic permeability; W_1 and W_2 are the effective turns of the torque winding and suspension winding, respectively.

3. COMPARISON OF PROPERTIES BETWEEN AMORPHOUS ALLOY AND SILICON STEEL

In recent years, soft magnetic materials have been used in modern electronic and electrical equipment which require high magnetic flux density and core loss, such as silicon steel and iron-based amorphous alloy. Silicon steel is a kind of silicon alloy steel with 1.0~4.5% silicon content and less than 0.08% carbon content. It has the characteristics of high magnetic conductivity, low coercivity, and large resistivity, so that the hysteresis loss and eddy current loss are small. Silicon steel is mainly used as magnetic materials in motors, transformers, electrical appliances, and electrical instruments.

Amorphous alloy is also called metallic glass or glass metal. The composition of its material molecules does not have regular periodicity in space, and there is no crystalline alloy grain, grain boundary. It is a new high technology magnetic conductivity material. This amorphous alloy has many unique properties, such as excellent magnetism, corrosion resistance, wear resistance, high strength, hardness and toughness, high resistivity, and electromechanical coupling properties [22–24]. Because of its excellent performance and simple process, it has been the focus of research and development of material science since the 1980s. Different from the traditional silicon steel sheet [25, 26], the physical characteristics of amorphous alloy material are thin, brittle, and hard, leading to stamping process

difficult and die wear fast, increasing process cost, so its production cost is relatively high. Therefore, amorphous alloy often exists in the form of winding process in practice.

Table 2 shows the performance parameters comparison of amorphous alloy material and silicon steel material. As can be seen from the table, the coercivity, hysteresis loss coefficient and iron consumption of amorphous alloy material are lower than those of traditional silicon steel material. And the density of the amorphous alloy is lower than that of the silicon steel, which means that the weight of the amorphous alloy material is lower than that of the silicon steel material for the same volume of the motor.

Table 2. Comparison of performance parameters of the two materials.

Parameters	amorphous alloy	silicon steel
Coercivity/($\text{A}\cdot\text{m}^{-1}$)	< 4	< 30
Hysteresis loss coefficient	1.4	179
Thickness / μm	25	350
Maximum permeability / 10^4	> 25	4
Specific resistance /($\mu\Omega\cdot\text{cm}$)	130	45
Density /($\text{kg}\cdot\text{m}^{-3}$)	7180	7700
The iron loss when the magnetic field alternating frequency is 100 Hz and the magnetic induction intensity is 1 T /(W/kg)	0.53	2.9

Figure 2 shows the magnetization characteristic curves of amorphous alloy material and silicon steel material, where H is the magnetic field intensity, and B is the magnetic induction intensity. Comparing the magnetization curves of the two materials, it can be seen that the magnetic permeability of silicon steel material is lower than that of amorphous alloy material. However, its saturation flux density is higher than that of amorphous alloy material.

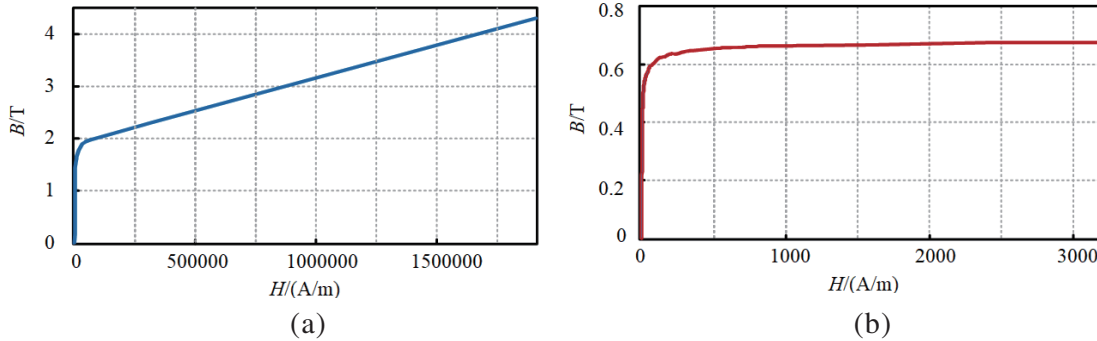


Figure 2. Magnetization curves of the two materials. (a) Magnetization curve of silicon steel. (b) Magnetization curves of amorphous alloy.

4. THE BL-IM MODELING AND MAGNETIC DENSITY DISTRIBUTION OF AMORPHOUS ALLOY MATERIAL

In order to observe the difference of magnetic conductivity of the two materials more intuitively, ANSYS is used to model two kinds of material motors. According to the actual structure of the motor, the motor model is drawn in ANSYS finite element software as shown in Fig. 3 and Fig. 4. The mesh is divided as shown in Fig. 5.

The magnetic flux density distribution is shown in Fig. 6 of BL-IM rotors with silicon steel and amorphous alloy materials, respectively. It can be seen from Table 2 that the magnetic conductivity

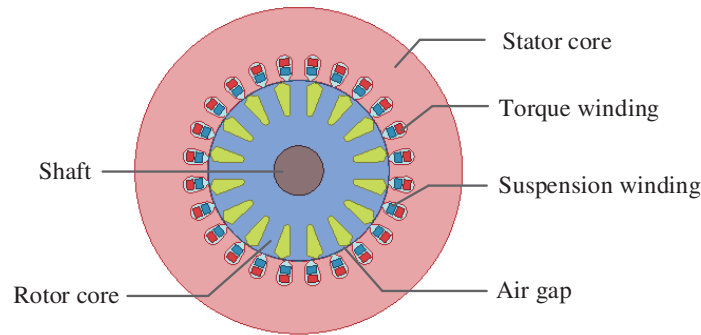


Figure 3. The BL-IM structure diagram.

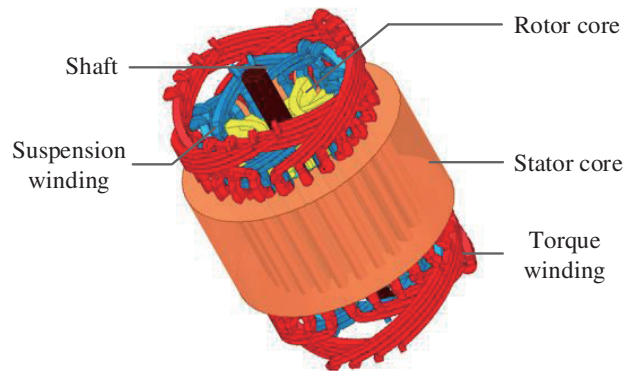


Figure 4. The BL-IM 3D finite element model.

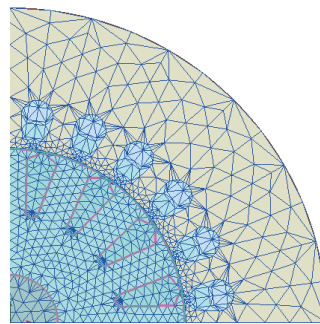


Figure 5. Mesh map of the BL-IM.

of amorphous alloy material is much higher than that of silicon steel material. The high magnetic conductivity indicates its good magnetic conductivity. Therefore, the magnetic induction intensity of amorphous alloy material is higher than that of silicon steel material near the rotating shaft.

5. PERFORMANCE VARIATION OF THE BL-IM USING AMORPHOUS ALLOY MATERIAL

In order to investigate the variation of motor performance caused by the BL-IM rotor using amorphous alloy material, ANSYS [27–29] is used to carry out finite element analysis of BL-IM rotor using silicon steel and amorphous alloy, under no-load operation and on-load operation, respectively. The torques, speeds, and the radial forces of x -axis and y -axis are compared to further observe the performance variation of the motor caused by the use of amorphous alloy material.

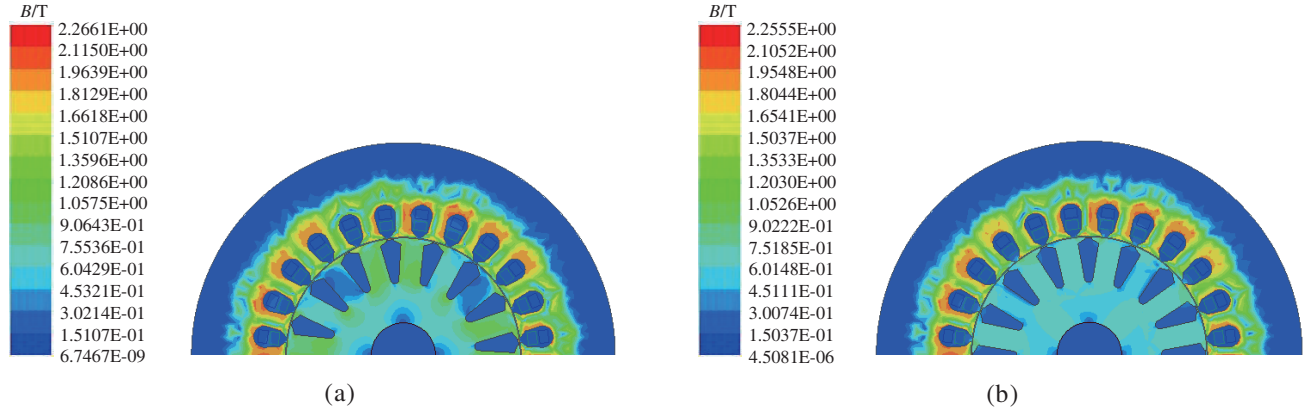


Figure 6. Distribution of magnetic flux density. (a) Magnetic density distribution of silicon steel rotor. (b) Magnetic density distribution of amorphous alloy rotor.

5.1. No-Load Operation

Figures 7–10 are the curves of torque, speed, and radial forces of the BL-IM at no-load operation and given speed $n = 1500$ r/min. The torque curves are shown in Fig. 7, and the rotors are made of silicon steel and amorphous alloy, respectively. According to the figure, the motor torque fluctuation range is between -28 N·m and $+53$ N·m when the rotor is made of silicon steel. When the rotor is made of amorphous alloy material, the torque fluctuation range of the motor is from -10 N·m to $+43$ N·m, and the fluctuation difference between up and down is smaller.

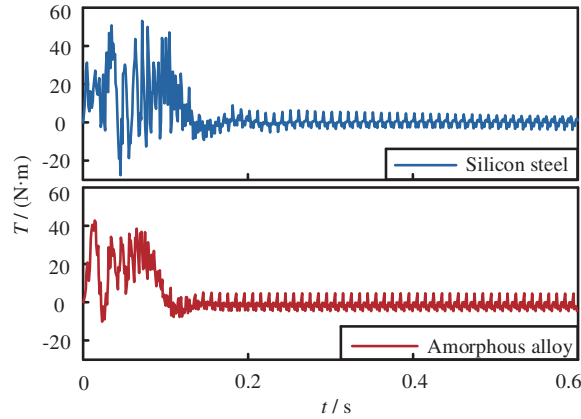


Figure 7. Torque curves under two materials.

According to the comparison of rotor speeds of two materials in Fig. 8, the speed of the silicon steel motor reaches the given value $n = 1500$ r/min at $t = 0.13$ s, and the overshoot is 3.7%. However, the speed of the amorphous alloy motor can reach the given value at $t = 0.1$ s, and the overshoot is 2.4%. By comparison, it can be seen that the speed of the amorphous alloy motor rises faster, and the overshoot is smaller. It is indicated that the amorphous alloy material has certain advantages in motor operation.

Different from traditional motors, the BL-IM also needs to consider the suspension performance of the rotor. That is the x -axis and y -axis radial forces and vibration amplitude of the rotor. The radial force waveforms of x -axis and y -axis are shown in Fig. 9 and Fig. 10 when silicon steel and amorphous alloy materials are used in the motor. As can be seen from the figure, the radial force fluctuation of the rotor with amorphous alloy material is smaller than that of the silicon steel motor during suspension. In particular, it can be seen from the x -axis radial force that the jitter of the amorphous alloy rotor is

less. Therefore, the vibration amplitude of the rotor can be reduced by the application of amorphous alloy rotor, and the rotor suspension is more stable.

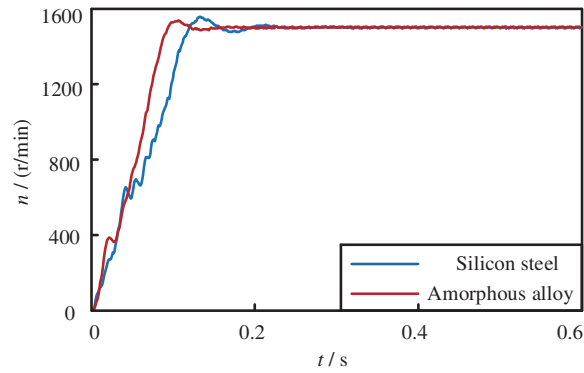


Figure 8. Speed curves under two materials.

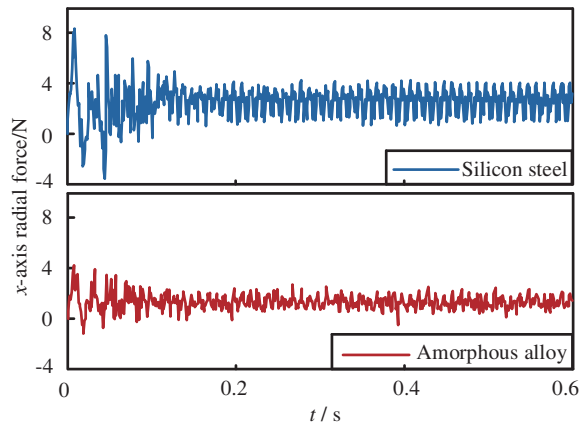


Figure 9. *x*-axis radial forces under two materials.

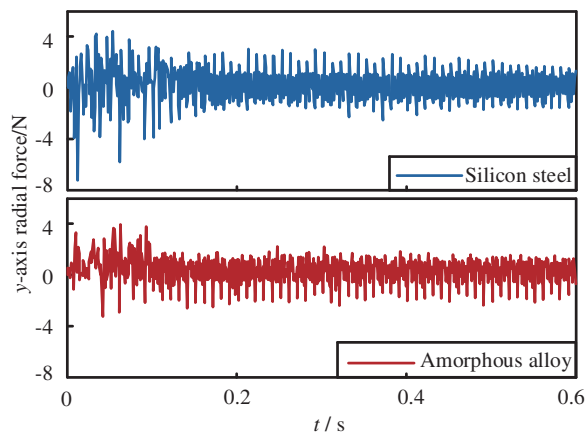


Figure 10. *y*-axial radial forces under the two materials.

5.2. On-Load Operation

Figures 11–13 are the curves of the torques, speeds, and radial forces of BL-IM at a given speed of $n = 1500$ r/min under a load of $5\text{N}\cdot\text{m}$. The torque curves are shown in Fig. 11, and the rotors are made of silicon steel and amorphous alloy, respectively. As can be seen from the figure, when the rotor is made of silicon steel, the motor torque fluctuation range is between $-30\text{N}\cdot\text{m}$ and $+53\text{N}\cdot\text{m}$, and the output torque reaches stability at about $t = 0.3\text{s}$. When the rotor is made of amorphous alloy material, the torque fluctuation range of the motor is from $-2\text{N}\cdot\text{m}$ to $+53\text{N}\cdot\text{m}$, and the output torque is stable at about $t = 0.12\text{s}$. By comparison, it is shown that the amorphous alloy material has better torque output characteristics.

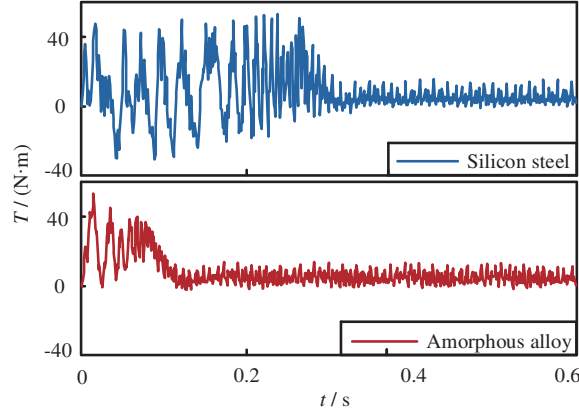


Figure 11. Torque curves under two materials.

According to the comparison of rotor speeds of two materials in Fig. 12, the speed of silicon steel motor reaches the given value at $t = 0.3\text{s}$. In the start-up stage, the speed rises slowly and fluctuates greatly. However, the speed of the amorphous alloy motor can reach the given value at $t = 0.11\text{s}$. The speed rise is smooth, and the fluctuation is small. By comparison, it can be seen that the speed of the amorphous alloy motor rises faster, and the fluctuation is smaller when the motor starts. It is indicated that the amorphous alloy material also has advantages when the motor runs with load.

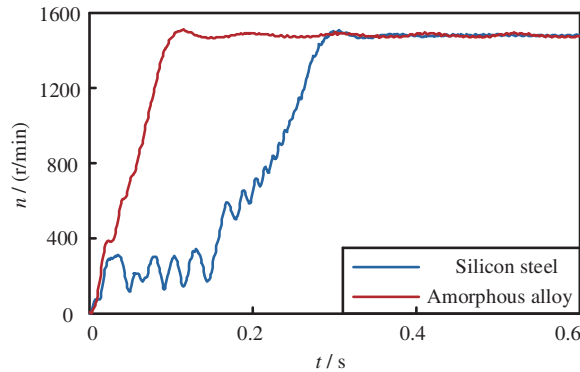


Figure 12. Speed curves under two materials.

Figures 13 and 14 show the x -axis and y -axis radial force waveforms of the motor using silicon steel and amorphous alloy materials. As can be seen from the figure, the radial force fluctuation of the amorphous alloy rotor is significantly smaller than that of the silicon steel motor in suspension at the start stage of the motor. The jitter amplitude of the rotor can be effectively reduced, and the rotor has better suspension performance.

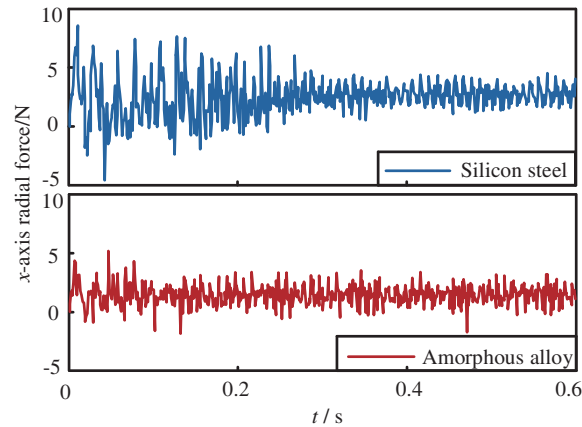


Figure 13. x -axis radial forces under two materials.

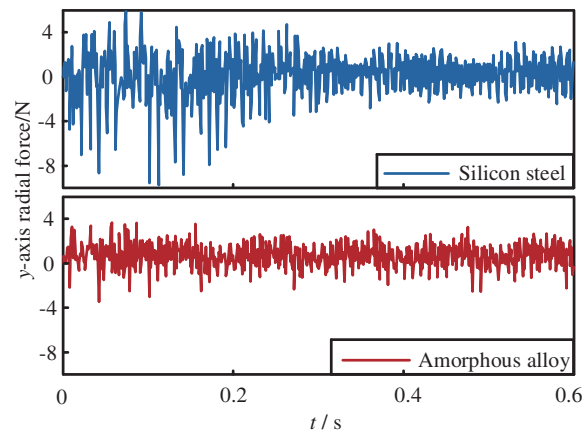


Figure 14. y -axis radial forces under the two materials.

6. CONCLUSION

The BL-IM electromagnetic property variation is studied which is caused by the application of amorphous alloy material to the rotor core. The rotor cores made of silicon steel material and amorphous alloy material are compared by finite element analysis. First of all, through the magnetic density distribution, the motor made of amorphous alloy material has better magnetic conductivity. Secondly, the torques, speeds, and radial forces of the two motors are compared in no-load operation and on-load operation environment. By comparison, the motor made of amorphous alloy material has smoother speed, faster rise, and smaller overshoot at the starting stage. At the same time, the x -axis and y -axis radial force fluctuations of the amorphous alloy rotor are smaller. The rotor vibration range is narrowed down, and the suspension is more stable. Therefore, the use of amorphous alloy material can effectively improve the operation characteristics and suspension performance of the BL-IM. Finally, combined with the characteristics of low loss and low density of amorphous alloy material itself, the loss and weight of the motor can be reduced, which is more conducive to meet the operation requirements of BL-IM in high speed and ultra-high speed, life science, and other special environments.

REFERENCES

1. Noh, M. and D. L. Trumper, "Homopolar bearingless slice motor with flux-biasing halbach arrays," *IEEE Transactions on Industrial Electronics*, Vol. 67, No. 9, 7757–7766, 2020.
2. Zhang, W. Y. and H. Q. Zhu, "Radial magnetic bearings: An overview," *Results in Physics*, Vol. 7, 3756–3766, 2017.
3. Turk, N., N. Bulic, and W. Gruber, "Nonlinear control of a bearingless flux-switching slice motor with combined winding system," *IEEE-Asme Transactions on Mechatronics*, Vol. 25, No. 1, 152–163, 2020.
4. Sun, X. D., Z. J. Jin, Y. F. Cai, et al., "Grey wolf optimization algorithm based state feedback control for a bearingless permanent magnet synchronous machine," *IEEE Transactions on Power Electronics*, Vol. 35, No. 12, 13631–13640, 2020.
5. Wang, H. J., F. X. Li, "Design consideration and characteristic investigation of modular permanent magnet bearingless switched reluctance motor," *IEEE Transactions on Industrial Electronics*, Vol. 67, No. 6, 4326–4337, 2020.
6. Yang, Z. B., C. L. Lu, X. D. Sun, et al., "Study on active disturbance rejection control of a bearingless induction motor based on an improved particle swarm optimization-genetic algorithm," *IEEE Transactions on Transportation Electrification*, Vol. 7, No. 2, 694–705, 2021.
7. Bu, W. S., X. W. Tu, C. X. Lu, et al., "Adaptive feedforward vibration compensation control strategy of bearingless induction motor," *International Journal of Applied Electromagnetics and Mechanics*, Vol. 63, No. 2, 199–215, 2020.
8. Yang, Z. B., C. Sun, X. D. Sun, et al., "An improved dynamic model for bearingless induction motor considering rotor eccentricity and load change," *IEEE Transactions on Industrial Electronics*, doi: 10.1109, 2021.
9. Chen, J. H., Y. Fujii, M. W. Johnson, et al., "Optimal design of the bearingless induction motor," *IEEE Transactions on Industry Applications*, Vol. 57, No. 2, 1375–1388, 2020.
10. Chiba, A., J. Asama, "Influence of rotor skew in induction type bearingless motor," *IEEE Transactions on Magnetics*, 2012, Vol. 48, No. 11, 4646–4649.
11. Xu, X. P., Q. K. Han, Z. Y. Qin, et al., "Analytical methods for the radial electromagnetic vibration of stator in permanent magnet motors with an amorphous alloy core," *Mechanical Systems and Signal Processing*, doi: 10.1016, 2020.
12. Li, Z. Z., S. X. Zhou, G. Q. Zhang, et al., "Highly ductile and ultra-thick p-doped FeSiB amorphous alloys with excellent soft magnetic properties," *Materials*, doi: 10.3390, 2018.
13. Ou, J., Y. Z. Liu, P. Breining, et al., "Experimental study of the amorphous magnetic material for high-speed sleeve-free PM rotor application," *IEEE Transactions on Industrial Electronics*, Vol. 67, No. 6, 4422–4432, 2020.
14. Azuma, D., N. Ito, M. Ohta, "Recent progress in Fe-based amorphous and nanocrystalline soft magnetic materials," *Journal of Magnetism and Magnetic Materials*, doi: 10.1016, 2020.
15. Liu, D. S., J. C. Li, R. K. Noubissi, et al., "Magnetic properties and vibration characteristics of amorphous alloy strip and its combination," *IET Electric Power Applications*, Vol. 13, No. 10, 1589–1597, 2019.
16. Qiao J., Yu P., Wu Y. X., et al., "Compact review of laser welding technologies for amorphous alloys," *Metals*, doi: 10.3390, 2020.
17. Tang, R. Y., W. M. Tong, and X. Y. Han, "Overview on amorphous alloy electrical machines and their key technologies," *Chinese Journal of Electrical Engineering*, Vol. 2, No. 1, 1–12, 2016.
18. Sun, X. D., L. Chen, H. B. Jiang, et al., "High-performance control for a bearingless permanent-magnet synchronous motor using neural network inverse scheme plus internal model controllers," *IEEE Transactions on Industrial Electronics*, Vol. 63, No. 6, 3479–3488, 2016
19. Chen, J. H., Y. Fujii, M. W. Johnson, et al., "Optimal design of the bearingless induction motor for industrial applications," *IEEE Transactions on Industry Applications*, Vol. 57, No. 2, 1375–1388, 2021.

20. Chen, Y. P., W. S. Bu, and Y. K. Qiao, "Research on the speed sliding mode observation method of a bearingless induction motor," *Energies*, doi: 10.3390, 2021.
21. Yang, Z. B., J. L. Ji, X. D. Sun, et al., "Active disturbance rejection control for bearingless induction motor based on hyperbolic tangent tracking differentiator," *IEEE Journal of Emerging and Selected Topics in Power Electronics*, Vol. 8, No. 3, 2623–2633, 2020.
22. Wang, Y. C., Y. Zhang, A. Takeuchi, et al., "Magnetic influence of alloying elements in Fe-rich amorphous alloys studied by ab initio molecular dynamics simulations," *IEEE Transactions on Magnetics*, Vol. 51, No. 11, 1–4, 2015.
23. Chai, F., Z. Y. Li, L. Chen, et al., "Effect of cutting and slot opening on amorphous alloy core for high-speed switched reluctance motor," *IEEE Transactions on Magnetics*, Vol. 57, No. 2, 1–5, 2021.
24. Ismagilov, F. R., L. Papini, V. E. Vavilov, et al., "Design and performance of a high-speed permanent magnet generator with amorphous alloy magnetic core for aerospace applications," *IEEE Transactions on Industrial Electronics*, Vol. 67, No. 3, 1750–1758, 2020.
25. Gao, L. Y., H. Zhang, L. B. Zeng, et al., "Rotor topology optimization of interior permanent magnet synchronous motor with high-strength silicon steel application," *IEEE Transactions on Magnetics*, Vol. 57, No. 2, 1–6, 2021.
26. Tong, W. M., S. H. Dai, S. N. Wu, et al., "Performance comparison between an amorphous metal PMSM and a silicon steel PMSM," *IEEE Transactions on Magnetics*, Vol. 55, No. 6, 1–5, 2019.
27. Chen, M., K. T. Chau, C. H. T. Lee, et al., "Design and analysis of a new axial-field magnetic variable gear using pole-changing permanent magnets," *Progress In Electromagnetics Research*, Vol. 153, 23–32, 2015.
28. Wen, Y., G. L. Li, Q. J. Wang, et al., "Modeling and analysis of permanent magnet spherical motors by a multitask gaussian process method and finite element method for output torque," *IEEE Transactions on Industrial Electronics*, Vol. 68, No. 9, 8540–8549, 2021.
29. Shi, Z., X. D. Sun, Y. F. Cai, et al., "Robust design optimization of a five-phase PM hub motor for fault-tolerant operation based on taguchi method," *IEEE Transactions on Energy Conversion*, Vol. 35, No. 4, 2036–2044, 2020.
30. Najafi, A. and I. Iskender, "Comparison of core loss and magnetic flux distribution in amorphous and silicon steel core transformers," *Electrical Engineering*, Vol. 100, No. 2, 1125–1131, 2018.
31. Li, L. J., S. H. Li, G. M. Li, et al., "Design and performance prediction of switched reluctance motor with amorphous cores," *Materials Research Innovations*, Vol. 19, S328–S332, 2015.